Continental collision with finite indenter strength:
1. Concept and model formulation

Jörg Robl and Kurt Stüwe

Institut für Erdwissenschaften, Universität Graz, Graz, Austria

[1] The partitioning of deformation during continental collision is modeled in plan view using a thin viscous sheet simulation. In contrast to many previous models, an indenter is defined here as a zone of finite viscosity contrast to the foreland and aspect ratio. Deformation is enforced by pushing the southern boundary into the model region. It is shown that deformation is equally partitioned between indenter and foreland if the aspect ratio of the indenter is about 1:2, and it is about twice as viscous as the foreland. For higher-viscosity contrasts between the two plates, the partitioning of deformation between indenter and foreland depends more strongly on Argand number. The process of lateral extrusion is investigated by separating the lateral velocity field into a component that is due to lateral escape and a component that is due to gravitational extensional collapse. It is shown that lateral escape is roughly constant over time and is controlled by the convergence velocity and the obliquity of indentation. **Citation:** Robl, J., and K. Stüwe (2005), Continental collision with finite indenter strength: 1. Concept and model formulation, *Tectonics*, *24*, TC4005, doi:10.1029/2004TC001727.

1. Introduction

[2] The process of continental collision is generally described with an indenter geometry: A rigid continent is assumed to indent into a softer continent producing a region of thickened crust and elevated topography in front of an undeformed block referred to as the indenter. This geometry has been assumed in analogue models for continental collision [e.g., *Tapponnier et al.*, 1982; *Ratschbacher et al.*, 1991; *Bonini et al.*, 1999], numerical models [*England and Houseman*, 1986; *Houseman and England*, 1993] and conceptual models made by field geologists [*Frisch et al.*, 2000; *Ratschbacher et al.*, 1989]. Indenter models for continental collision have been applied to field observation from a number of orogens, in particular the European Alps and the India-Asia collision zone. In the India-Asia collision zone, this model has brought wide success explaining, for example, the process of continental extension in regimes of overall convergence [*Houseman and England*, 1986;

England and Houseman, 1986]. More recent refinements of this model have considered variable rheologies within the deforming plate [e.g., *Neil and Houseman*, 1997], but the indenter itself has usually been described as rigid by imposing the model boundary at the indentation front. For the India-Asia collision zone this assumption appears valid as the majority of shortening has been compensated by deformation within the Asian plate [*Molnar and Tapponnier*, 1975] (Figure 1a).

[3] In contrast, in the European Alps, both the Adriatic indenter and the European foreland show significant deformation and elevated topography (Figure 1b). Significant parts of the Adriatic plate have surface elevations comparable to the region of highest topography of the European plate including the Dolomites and other parts of the Italian and Slovenian Alps. In fact, while the Adriatic "indenter" may have been rigid in the Oligocene, the majority of the current seismicity now occurs within the Adriatic plate [*Bressan et al.*, 1998]. Clearly, the present-day distribution of deformation between the two plates is a consequence of significant changes of the orogen through time and the inherently three-dimensional nature of the collision process. Nevertheless, two-dimensional numerical modeling of the Alpine orogen on cross sections has been extremely successful in explaining features like the distribution of deformation between the two plates, or the depth dependence of deformation [e.g., *Beaumont et al.*, 1996; *Pfiffner et al.*, 2000; *Gerbault and Willingshofer*, 2004]. On the other hand, such models cannot explain fundamental plan view features like the lateral escape of the orogen to the east [*Ratschbacher et al.*, 1991].

[4] In this study we use a simple finite element simulation to investigate the influence of the indenter rheology on the distribution of deformation between two plates in two-dimensional plan view. In this, the first of two companion papers, we explore a range of critical parameters that influence the lateral displacement and vertical strain rate fields. In particular, we explore the influence of the shape and rheology of the indenter on the process of lateral extrusion during continental convergence. The results are roughly compared to some large-scale observations from the India-Asia collision zone and the Eastern Alps. In a companion paper we use a more refined plan view model to calculate strain, stress and velocity pattern in the Alpine realm for a variety of different rheological models and apply the model directly to the lateral extrusion of the Eastern Alps [*Robl and Stüwe*, 2005]. Data and model are compared to place constraints on the rheology contrast between
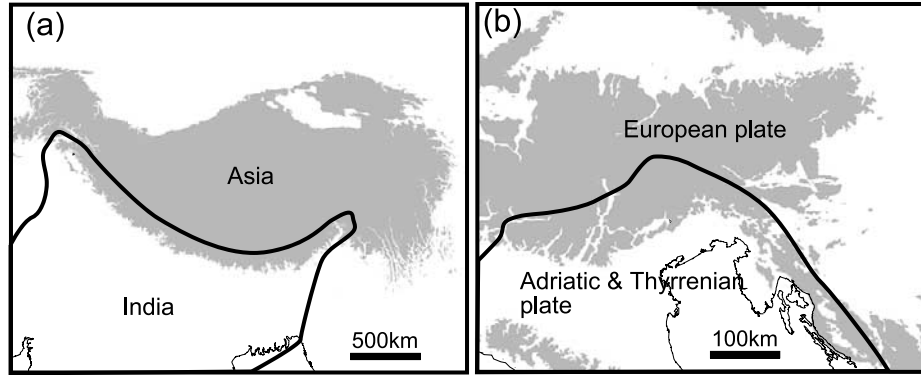
Figure 1. Comparison of the position of the plate boundary with the region of elevated topography for two orogens. Solid curves indicate the plate boundaries schematically after *Harrison et al.* [1992] and *Babbucci et al.* [2004]. (a) Plate boundary in the India-Asia collision zone. Most of the elevation above 3000 m (shaded region) occurs within the Asian plate. (b) Adriatic plate−European plate collision zone. Shaded region is the area above 600 m surface elevation. Both plates show significant elevation.

Adriatic and European plates and its evolution through time.

2. Model Formulation

[5] In our model we describe continental collision with a thin viscous sheet approach in which the indenter is a region of finite size and rheology along one side of a two-dimensional model continuum. We follow the thin sheet approach initially described by *Bird and Piper* [1980] and *England and McKenzie* [1982] and successfully used by *Houseman and England* [1986] and *England and Houseman* [1986] and several others [e.g., *Sobouti and Arkani-Hamed*, 1996; *Marotta et al.*, 2002; *Soofi and King*, 2002]. Within this model, we assume that tractions on horizontal planes are negligible and that a nonlinear viscous constitutive relationship of the following form applies:

$$\tau_{ij} = B\dot{E}^{\left(\frac{1}{n}-1\right)}\dot{\varepsilon}_{ij}. \tag{1}$$

In this power law rheology, τ_{ij} and $\dot{\varepsilon}_{ij}$ are the components of the two-dimensional deviatoric stress and strain rate tensor, respectively, where the subscripts i and j represent the horizontal x and y directions as shown in Figure 2a. In this paper we refer to the x and y direction also in terms of the geographic directions west, east, north and south. $\dot{E}$ is the 2nd invariant of the strain rate tensor and n is the power law exponent. The proportionality constant B incorporates all material- and temperature-dependent terms. It is equivalent to 2 times the viscosity ($B = 2\eta$) if $n = 1$; that is, the viscous flow is Newtonian. However, for $n \neq 1$, B is only a pre-exponent constant. Then, the viscosity is strain rate–dependent, and only an effective viscosity can be defined from equation (1) from the ratio of stress and strain rate. However, the rheology contrast between different parts of the continuum can be described by $\eta = B^n$, if it is defined as the rheology contrast between two regions deforming

under the same stress (see *Tenczer et al.* [2001] for detailed explanation). Thus a rheology contrast of $\eta = 100$ between indenter and foreland at $n = 3$ can be described by setting $B = 4.642$ (because $\eta = 4.642^3 = 100$). Although these numbers are dimensionless in the model, they scale directly with real viscosity contrasts; for example, $\eta = 100$ may be interpreted as a contrast of 10^{23} Pa s in the indenter to 10^{25} Pa s in the foreland.

[6] Strain rate is defined in terms of the velocity gradients

$$\dot{\varepsilon}_{ij} = \frac{1}{2}\left(\frac{\delta u_i}{\delta_j} + \frac{\delta u_j}{\delta_i}\right), \tag{2}$$

where u is velocity, and the i and j refer to the Cartesian coordinates as above. The dimensionless force balance equations in the thin viscous sheet formulation are given by [*England and McKenzie*, 1982]

$$\frac{\delta\tau_{ij}}{\delta_j} - \frac{\delta\tau_{zz}}{\delta_i} = \frac{Ar}{2}\frac{\delta S}{\delta_i}, \tag{3}$$

where S is the reference crustal thickness (for which we assume $S = 35$ km), τ_{zz} is the vertical principal deviatoric stress and Ar is the Argand number. The right hand side of equation (3) is a term opposing thickening of the crust because of buoyancy forces. The Argand number may be physically interpreted as

$$Ar = \frac{gL\rho_c(1 - \rho_c/\rho_m)}{B(U_0/L)^{(1/n)}}, \tag{4}$$

where g is the gravitational acceleration, ρ_c and ρ_m are the crustal and mantle densities, U_0 is a representative horizontal velocity of the collision process (the velocity of the southern boundary in our model) and L is the thickness of the lithosphere (for which we assume $L = 100$ km).
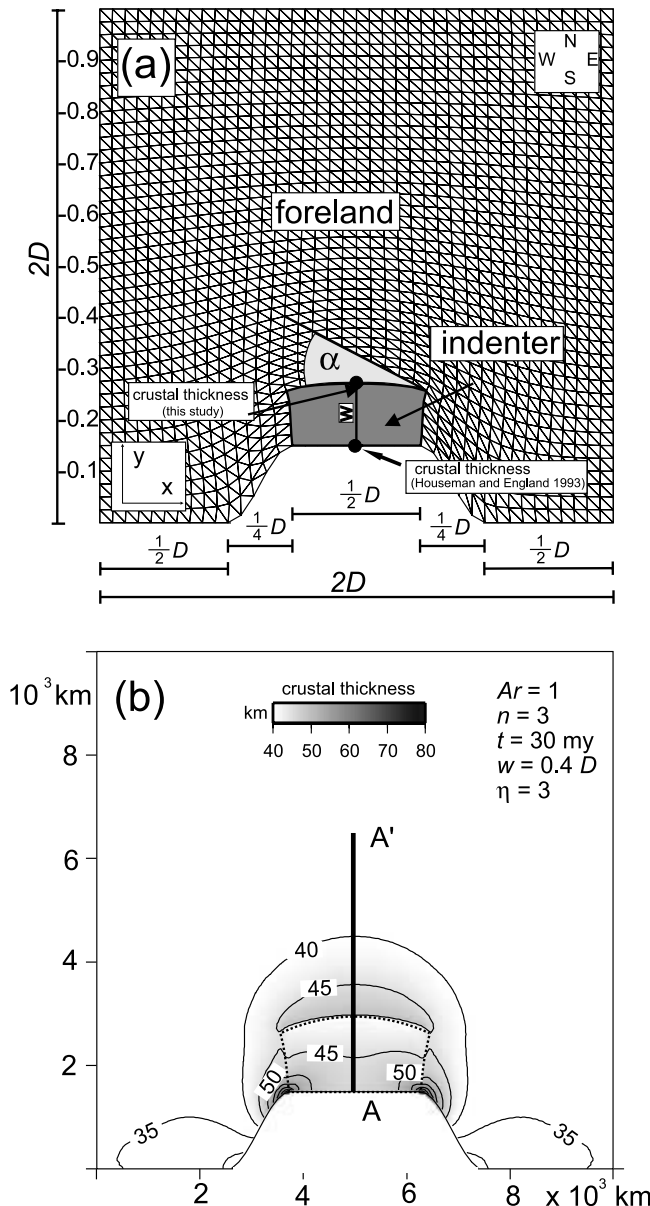
Figure 2. Model geometry and boundary conditions. (a) Regular mesh consisting of 3200 triangles. The shaded region is referred to as the "indenter" and the light region as the "foreland." All features, such as box dimensions, indenter width, indenter length, and length of the taper functions, are defined in terms of D. Arrows indicate the points where crustal thickness is measured during convergence in this study and the study by *Houseman and England* [1993]. Indentation angle α is defined in the text. Directions are referred to in the text with x and y or with north, south, west, and east (see insets). (b) Typical model result scaled for a nominal length scale of D = 5000 km for w = 0.4D, α = 0 (indenter is outlined with the dotted curve), and a nominal indentation velocity of 5 cm per year. Note that the crustal thickening is distributed between the indenter and the foreland. The vertical line A-A′ shows the position of the profiles shown in Figure 4.

For n = 1 and by combining the physical constants into C = g ρ_c (1 − ρ_c/ρ_m), equation (4) may be simplified to

$$Ar = \frac{CL^2}{2\eta U_0},\tag{5}$$

where $C \approx 3418$ kg m^{-2} s^{-2} for $\rho_c = 2700$ kg m^{-3}, $\rho_m = 3100$ kg m^{-3} and $g = 9.81$ m s^{-2}. In this form it may be seen that the Argand number can be interpreted as the ratio of vertical and horizontal stresses. It is a measure of the tendency of an orogen to collapse under its own gravitational potential energy. At high Argand numbers ($Ar > 3$) an orogen tends to flow apart at the same rate it is built by the indentation process, so that no appreciable topography can be developed. In contrast, for small Argand numbers ($Ar < 3$) substantial amounts of potential energy may be stored in the orogen through crustal thickening. $Ar = 0$ implies that no gravitational forces act upon the orogen. In order to solve the set of equations we used the finite element method as implemented in the code BASIL of *Barr and Houseman* [1996]. All results are given in nondimensional form, but are scaled here for nominal values that can be compared directly to those chosen by *Houseman and England* [1993].

2.1. Geometry and Boundary Conditions

[7] For our considerations we choose initially a simple model geometry that can be compared directly with *Houseman and England* [1993] (Figure 2). This simple model is later expanded to explore additional parameters and a much more refined model is used in the parallel paper for our application to the Alps [*Robl and Stüwe*, 2005]. Here, we consider a quadratic region of a thin viscous sheet with side length 2D (nominally the side length is 10000 km or D = 5000 km). The eastern, northern and western boundaries are defined to be rigid by setting the normal and tangential velocities to zero along each of these boundaries. Along the southern boundary, a central section of the boundary of width D/2 is moving north with the velocity U_0 (here scaled to be 5 cm/year). On both sides of this central region, the velocity decreases with a cos² taper of length D/4 to zero. The tangential velocity along the entire southern boundary is set to zero.

[8] This geometry is almost identical to the "elongate geometry" of *Houseman and England* [1993], which differs only in having a slightly different aspect ratio of 1:0.9195. However, our geometry differs substantially in our description of the indenter. We describe the indenter as a central block of west-east length D/2 and north-south width w that is pushed northward by the moving part of the southern boundary (Figure 2a). As all calculations are performed dimensionless and the indenter is far removed from the model boundaries, the indenter can also be characterized by its aspect ratio 2w/D. This region is assumed to have a rheology contrast η with the foreland. It may be interpreted as a zone of active deformation within the indenting plate. Here, we refer to this zone as "the indenter" and the region in front of it as "the foreland" (Figure 2a), whereas *Houseman and England* [1993] referred only to the bound-
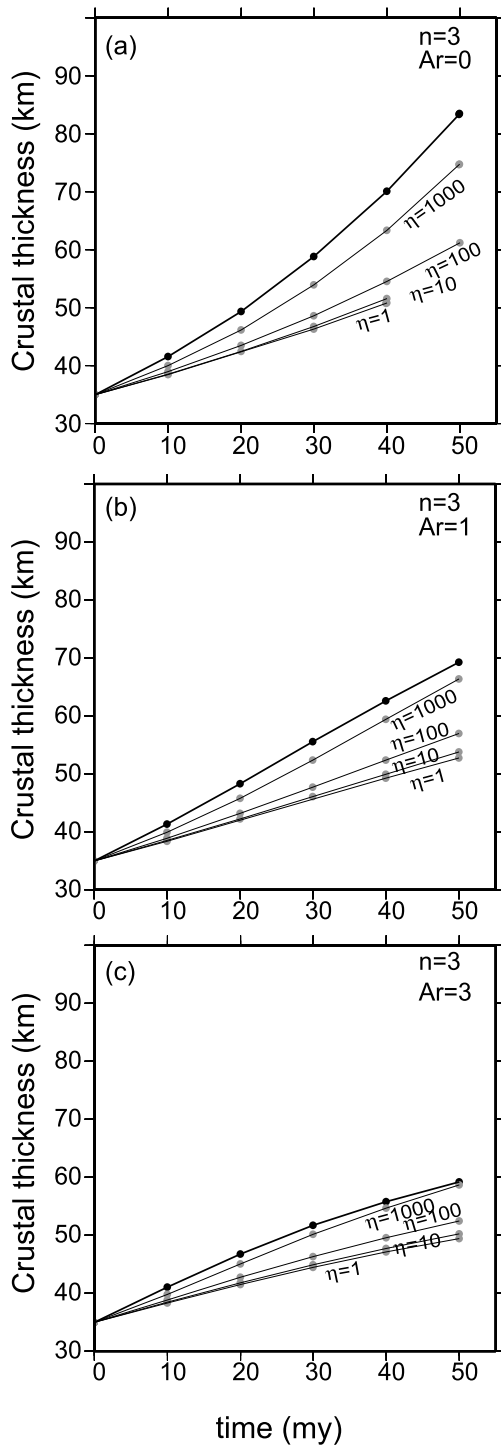
Figure 3. Variation of crustal thickness with time (gray dots and thin curves) in comparison with the model of *Houseman and England* [1993] (black dots and thick curves as in their Figure 7a) for three different *Ar* and *n* = 3. The crustal thickness is taken from a characteristic point (the midpoint) of the indenter front (see Figure 2 for detailed explanations).

ary itself (and the region outside the model region) as the indenter.

[9] The entire region was modeled with two regular types of meshes that match to the finite element mesh used by *Houseman and England* [1993]. We also used mesh generation routine of the program TRIANGLE [*Shewchuk*, 2002] to randomly triangulate meshes. Calculations were typically performed with a resolution of 80 × 80 elements so that the average area of one element is $0.0013D^2$ or 31250 km^2. Finite time calculations were done for nominal times of 50 m.y. (i.e., until the southern boundary has moved one quarter through the model region). Reproducibility of the results was ensured by comparing results with those for finer and coarser meshes. A larger number of elements results in a quadratic increase in the computation time but does not significantly increase the accuracy of the model. Figure 2b shows a general result where it may be seen that the thickening is distributed between the indenter and the foreland.

2.2. Comparison With Earlier Studies

[10] Distributed deformation between indenter and foreland as shown in Figure 2b has previously been modeled and interpreted by various authors, for example *Royden* [1996] or *Shen et al.* [2001]. However, these authors used a three-dimensional model that was confined to a Newtonian rheology and interpreted the distribution of deformation between indenter and foreland predominantly as a function of rheological variations between upper and lower crust or crust versus upper mantle. In view of our aim here to describe the partitioning of deformation in two dimensions, these studies do not suit a direct comparison. Other models investigating the partitioning of deformation between indenter and foreland include the analogue models of *Keep* [2000] and *Willingshofer et al.* [2004], but a careful numerical study investigating the controlling parameters for the distribution of deformation has not been performed. In order to interpret our results properly, we begin therefore with a comparison of our model with that of *Houseman and England* [1993], which can be described with our model as the end-member where for $\eta = 1$ or for $w = 0$. To quantify the evolution of thickness and its spatial distribution through time, it is useful to choose a specific point of the continuum that is characteristic of the general behavior of the solution region. For this, *Houseman and England* [1993] selected the midpoint of the southern boundary (midpoint of the indenter in their terminology). Correspondingly, we choose to observe the midpoint of the indenter in our own terminology, which is located a distance w from the southern boundary (Figure 2a). Figure 3 shows the thickness evolution of both points for a range of viscosity contrasts and using $w = D/4$ and $n = 3$ in all examples shown. The thick black solid lines and dots show the thickness evolution of the midpoint of the southern boundary (using no rheology contrast inside the model region, that is, $\eta = 1$). They are identical to those shown in Figure 7a of *Houseman and England* [1993]. It may be seen that the crustal thickening curve is convex toward the time axis when no gravity acts (i.e., $Ar = 0$, Figure 3a). This is because the thickening strain
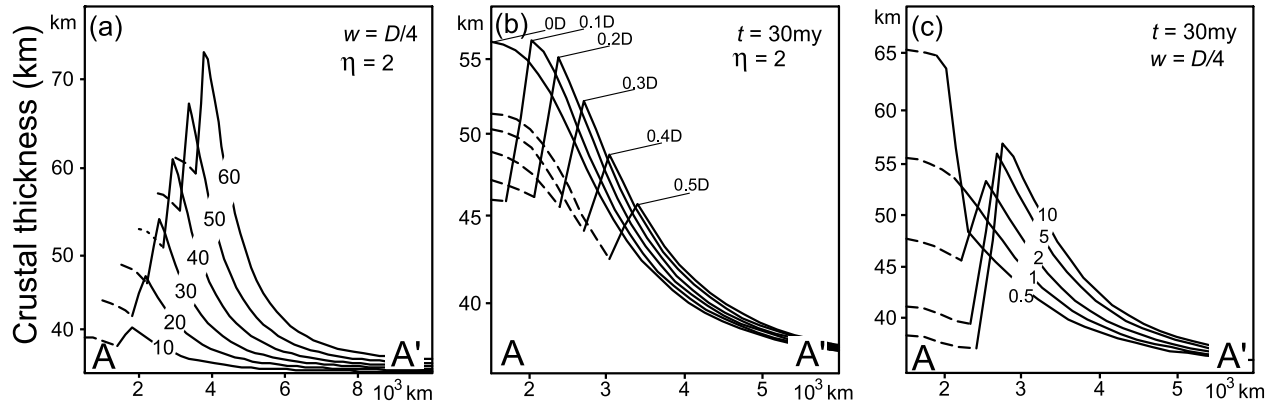
Figure 4. North-south profiles of crustal thickening as shown (profile A-A′) in Figure 2b. The diagrams show the distribution of thickening between indenter (dashed curves) and foreland (solid curves) as a function of time t, width of the indenter w, and viscosity contrast η. Argand number and power law exponent are $Ar = 1$ and $n = 3$ for all model calculations. (a) Increase of crustal thickness with elapsed time of convergence. Curves are labeled in million years. The different starting points of the profiles at different time steps result from the northward migration of the southern boundary. (b) Crustal thickness after 30 m.y. as a function of the width of the indenter labeled in multiples of D. (c) Crustal thickness as a function of η after 30 m.y. of convergence; η ranges from 0.5 to 10.

rate simply reflects the exponential increase in strain for constant convergence rate as the southern boundary gets closer to the northern boundary. Curves become concave toward the time axis for larger Argand numbers as gravity has an increasingly large effect on the thickening rate when deformation progresses and topography develops.

[11] These solid black lines are only partly matched by the thickening rate at the front of the indenter for $\eta = 1000$. Such a high viscosity contrast implies a practically rigid indenter so that the difference relative to the curves of *Houseman and England* [1993] must stem from the difference between the geometry of the indenting block used here (rectangular in shape) and the geometry of the indenting boundary used by *Houseman and England* [1993] (with a taper on both sides). The difference amounts to 8 km thickness difference after 50 m.y. for $Ar = 0$. The difference is smaller for larger Argand numbers as thickening is partly counteracted by gravitational collapse. For lower rheology contrasts of $\eta = 100$ and $\eta = 10$, crustal thickening rates decrease as the deformation becomes increasingly distributed between the indenter and the foreland. Similarly, the difference in crustal thickening between indenters of different rheologies becomes smaller for larger Ar. At $Ar = 3$, the influence of the indenter rheology on crustal thickening is small compared to the influence of gravitational collapse. As a consequence, there is a mere 10 km thickness difference (after 50 m.y.) between the foreland of very hard indenters and the foreland in a continuous medium with no rheology contrast ($\eta = 1$, Figure 3c). The high Ar determines that only small amounts of potential energy can be stored in the orogen during crustal thickening.

3. Model Results

[12] Aside from the rheology of the indenter, we have explored the consequences of changing two parameters on the stress and velocity field around the indenter: the width

of the indenter w and the angle of indentation α. Both parameters are known to have a fundamental influence on the deformation field in orogens. The width of the actively deforming zone in the foreland of orogens has a critical spatial relationship to the internal regions of the orogen [e.g., *Beaumont et al.*, 1996] and the angle of indentation is known to have a fundamental influence on orogenic development [*Platt*, 1993]. In fact, in the Eastern Alps, the angle of indentation has been considered as a primary parameter controlling the lateral escape [e.g., *Frisch et al.*, 1998, 2000]. The consequences of varying indentation angle and width are explored in terms of their influence on crustal thickening rate and horizontal displacement fields.

3.1. Influence of Indenter Size on Crustal Thickening

[13] In two-dimensional plan view, partitioning of deformation between two plates can only be described by defining an indenter of finite size and rheology. Then, the partitioning of deformation varies, depending on the width of the indenter and the rheology contrast between the indenter and the foreland. Figure 4a illustrates this partitioning for an indenter width of $w = D/4$ and a rheology contrast of $\eta = 2$ (and using $Ar = 1$ and $n = 3$). Figure 4a shows the temporal evolution of crustal thickening as seen on a north-south cross section through the orogen. Although the indenter is 2 times harder than the foreland, significant crustal thickening can be observed within the indenter (dashed part of lines). Maximum thickening within the indenter is near its southern boundary with a gradual decrease toward the indenter front. The maximum thickening in the indenter occurs along its southern boundary because the driving force for the northward motion of the indenter is given by the northward moving southern boundary. In essence, the southern boundary has a similar effect on the indenter as the indenter has on the foreland. At the
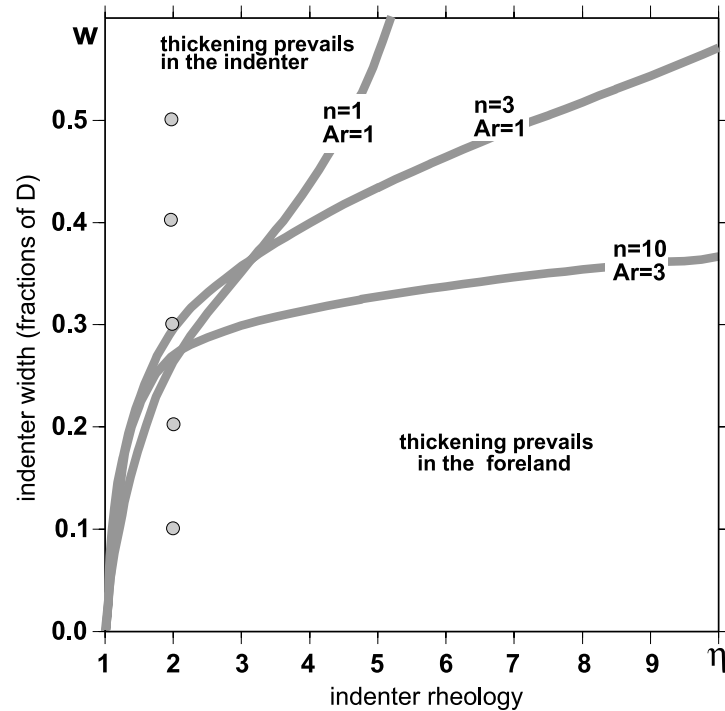
Figure 5. Diagram illustrating the partitioning of crustal thickening between indenter and foreland as a function of viscosity contrast η and the width of the indenter w. The contours show where the maximum thickening in both the indenter and the foreland is equal. The gray dots refer to points for which curves are shown in Figure 4b. Contours are shown for a time of 30 m.y. but are largely independent of time.

boundary of the indenter to the foreland the crustal thickness reaches its second and highest maximum just inside the foreland. From that point on the crustal thickness decreases northward to the initial value of 35 km (Figure 4a). After 50 m.y. the maximum thickness in the foreland is about 75 km and about 62 km in the indenter. The ratio of the maximum thickness in the foreland to that in the indenter is about 1.2:1. Because of the small Argand number this thickness ratio is largely independent of time. The region with a significantly thickened crust (>50 km) expands continuously with elapsed time.

[14] The thickness ratio between foreland and indenter changes dramatically with w (Figure 4b) and η (Figure 4c). In general, wide and soft indenters will compensate most of the shortening while the foreland remains only moderately deformed. In contrast, narrow and rigid indenters will transmit forces into the foreland and cause most of the deformation to occur in the foreland. Figure 4b shows that the crustal thickness (and thickening rate) is the same in foreland and in the indenter if the indenter has a width between $w = 0.3\,D$ and $w = 0.4D$ corresponding to an aspect ratio between width and length of 0.6 to 0.8 (using $\eta = 2$, $n = 3$, $Ar = 1$). At larger w (aspect ratio), the crustal thickness maximum is in the indenter, at smaller w, the thickness maximum is in the foreland. For $w = 0$ the distribution of thickness is equivalent to the model of *Houseman and England* [1993]. This result changes dramatically for other viscosity contrasts (Figure 4c). More rigid indenters will transmit stresses better into the foreland,

while softer indenters ($\eta < 1$) are highly deformed and most of the crustal thickening happens within the indenter. This process is amplified with an increasing width of the indenting block. Curves for $\eta = 1$ are equivalent to the results of *Houseman and England* [1993].

[15] The influence of indenter width and rheology on the distribution of thickening can be simultaneously explored on a diagram in which the indenter width is plotted against its rheology. This diagram can be contoured for the ratio of maximum crustal thickness in the indenter to that in the foreland (Figure 5). In Figure 5 the only the contour shown is that where the maximum thickening in the indenter is the same as that in the foreland (thickness ratio is 1). This contour is shown for three pairs of Ar and n that were suggested by *Houseman and England* [1993] to cover a representative range of Argand numbers and power law exponents for many orogens. The contours are shown for a time step at 30 m.y. but their position and shape is largely independent of time (see also Figure 4a). To the left and top of the contours (large w and small η) crustal thickening in the indenter exceeds that in the foreland; to the right and below the contours (small w and large η), crustal thickening in the foreland exceeds that in the indenter. All contours merge at $\eta = 1$ and $w = 0$, where the model becomes equivalent to that of *Houseman and England* [1993]. The three explored rheologies show only substantially different behavior above $\eta = 2$ and $w = 0.3D$. Increasing n has the general effect of localizing deformation [e.g., *Barr and Houseman*, 1996]. However, increasing
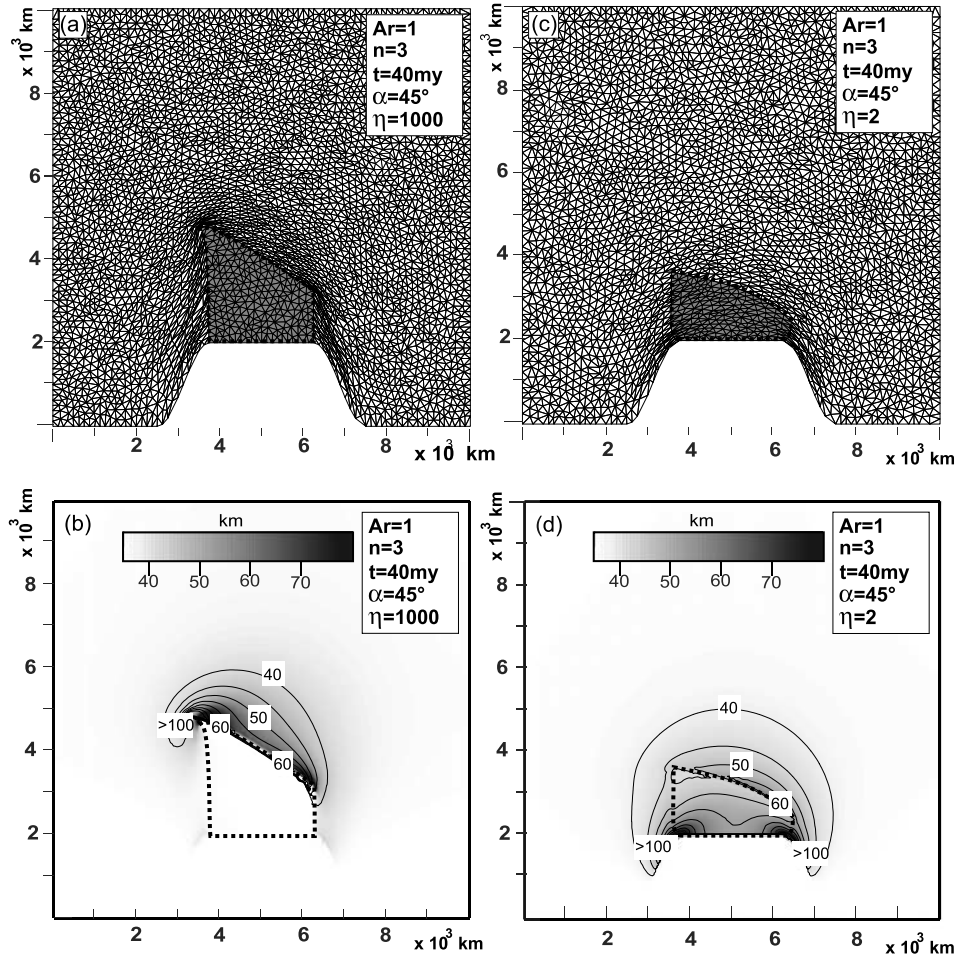
Figure 6. Influence of viscosity contrast on the evolution of oblique indenters. In both model runs, the geometry was initially identical, and $Ar = 1$, $n = 3$, and $\alpha = 45$. The bold dotted line is the outline of the indenter. (a and b) Viscosity contrast $\eta = 1000$. (c and d) Viscosity contrast $\eta = 2$. Figures 6a and 6c show the finite element mesh after 40 m.y. of nominal time. Figures 6b and 6d show the corresponding diagrams contoured for crustal thickness.

Ar has the effect of distributing the deformation. Thus, with increasing n and higher Ar, the width of the indenter becomes more important while changes in η have minor effect on the results. In contrast, at $n = 1$ only a little change in η shifts the results significantly, but these model runs are robust toward changes of w.

3.2. Influence of Indenter Shape on Distribution of Deformation

[16] Most indentation models assume indenters with an indenter front that is normal to the direction of indentation. However, many orogens, for example the European Alps, have differently shaped indenter fronts (Figure 1b). We therefore explored the influence of the angle of the indenter front with the direction of indentation, α, on the deformation field. This oblique indentation geometry is illustrated in Figure 2a. During all model runs, α was varied using a constant indenter width of $w = D/4$ corresponding to

1250 km in our scaled example. Because of the obliquely shaped indenter front, regular meshes could not be employed and all calculations were done with a randomly triangulated mesh.

[17] Different deformation patterns can best be explored if the indenter is virtually undeformable. A viscosity contrast of $\eta = 1000$ was therefore set (Figures 6a and 6b). Then, the angle of the indenter remains fairly constant during the whole collision. Only the northwestern tip shows some deformation (Figure 6a). Significant deformation occurs all around the indenter. The biggest shortening rates in the y direction are found directly north of the indenter, especially in front of the northwestern tip. A shortening maximum is also found at the northeastern edge. This shortening is directly reflected in thickening as shown in Figure 6b. The whole region in front of the indenter shows thickening with maximum values at the eastern and western edge. Extremely thickened crust up to 120 km occurs north of the western tip of the indenter. In front of the eastern edge
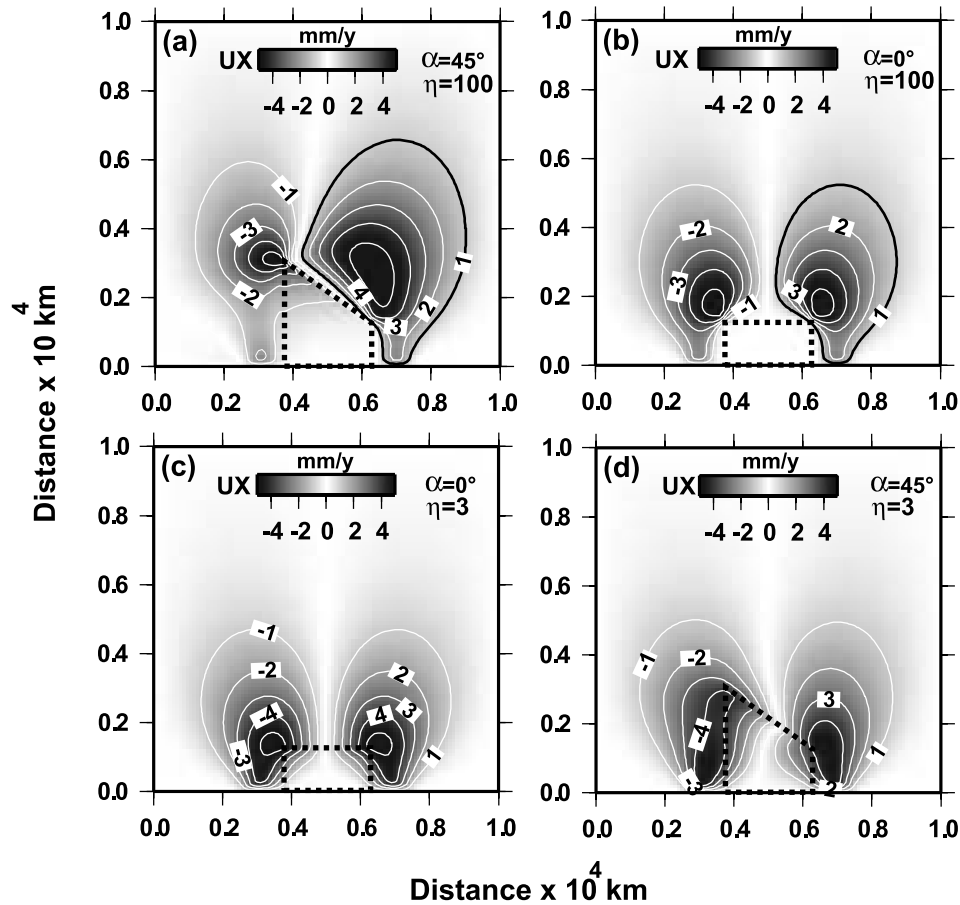
Figure 7. Instantaneous lateral displacement field during indentation for two different indenter rheologies: (a and b) $\eta = 100$ and (c and d) $\eta = 3$ and for two different indenter angles ($\alpha = 0°$ and $\alpha = 45°$). Contours for velocity in the x direction (u_x) are scaled using the nominal convergence rate of 5 cm per year. The bold dotted line outlines the indenter. Domains with maximum u_x are black, and west directed velocities are indicated with the negative. Contour interval is 1 mm per year. The two black contours in Figures 7a and 7b show the areas explored in more detail in Figure 10. Note that the eastward moving area is significantly larger for the oblique indenter in Figure 7a.

of the indenter the crust is thickened to around 100 km. Between these two maxima the region in front of the indenter is thickened to between 60 km to 70 km. Although the overall distribution of thickened area is oblique, it is generally similar to that around a square indenter with $\alpha = 0$ (e.g., Figure 2; see also *Houseman and England* [1993]). In contrast to the distribution of thickening, the horizontal velocity field is highly asymmetric for large α (Figure 7). For $\alpha = 45°$ a large corridor with east directed u_x opposes a small corridor with west directed u_x (Figure 7a). In comparison to the symmetric horizontal velocity field around rectangular indenters (Figure 7b), the area with significant east directed movement has about doubled, while the area moving west has about halved. Nevertheless the maximum values for u_x (denoted as u_x^{max}) are in the same order of magnitude in both corridors. This is caused by steeper gradients in the smaller west directed corridor and a smoother increase of u_x from the indenter to the maximum value in foreland in the east directed corridor. Despite the

high viscosity contrast ($\eta = 100$) the indenter shows some internal velocity especially at the western tip.

[18] In contrast to the oblique indenters of high viscosity contrasts to the foreland ($\eta = 100$ or above) somewhat softer indenters are rapidly deformed to become gradually symmetric during progressive deformation (Figures 6c and 6d). The angle of the indenter plays only a minor role for the crustal thickening during progressive deformation if the viscosity contrast is below 10. This is illustrated in Figures 6c and 6d for an indenter that is only 2 times more viscous than the foreland and has an initial convergence angle of $\alpha = 45$. It may be seen that this angle declines dramatically over time, caused by different shortening rates in the y direction at the eastern and the western end of the indenter (Figure 6c). The collision geometry alters gradually over time from oblique to straight as most of the deformation occurs within the indenter. Maximum crustal thickness up to 120 km (or 3.1 times the defaults crustal thickness of 35 km) occurs within the indenter if the indenter is weak

(η = 2) (Figure 6c). A second maximum up to 65 km can be observed in front of the indenter, with highest values at the eastern edge. In front of the indenter there is also shortening in the y direction and stretching in x direction. Crustal thickness declines only slightly from east to west. Correspondingly, Figure 7c shows that the horizontal velocity field for a rectangular indenter is not all this different from that of an indenter with an angle of $\alpha = 45°$, if the rheology contrast is around $\eta = 3$. Shape, size and maximum values of the east and west directed corridor are similar in Figures 7c and 7d. The material flow in the x direction occurs in the indenter and in the foreland. In summary, the indentation angle α plays an important role on the asymmetry of the lateral displacement if the viscosity contrast between indenter and foreland is larger than 10. It can be neglected if the viscosity contrast is significantly below 10.

4. Discussion

[19] The results presented above were calculated with a very simplistic model and using nondimensional values for all parameters. Before discussing some implications of the model we therefore feel that it is important to highlight some of the model limitations. First, like all thin sheet models, the model is quasi-two-dimensional, where the crustal thickness is evaluated as a variable and is used to calculate a potential energy function, but cannot be used to estimate any vertical gradients of velocity or stress. Thus it may be difficult to apply the model to areas where the velocity and thickening field is inherently related to the three-dimensional geometry of collision. For that reason we cannot consider continental subduction that would mitigate the deformation of the indenter. Nevertheless, as for two-dimensional models performed on cross sections, we argue that our results explore the controlling processes of a two-dimensional end-member of the collision process. Secondly, in our model, predictions for crustal thickening are based on the assumption of local isostasy. This may be critical for rigid indenters, where local maxima for crustal thickening in front of the indenter can exceed 120 km and there are steep gradients in crustal thickness. In that case models including "plate bending" might be more suitable [*Medvedev and Podladchikov*, 1999]. Thirdly, the model results were obtained for an incompressible viscous continuous material. As such, no consideration was given for all other deformation mechanisms or uncoupling between the indenter and the foreland as is observed at several first order fault systems like the Periadriatic fault system in the Alps [e.g., *Viola et al.*, 2001], or the Indus-Zangpo suture zone in the India-Asia collision zone. Finally, lateral viscosity contrasts are fixed over time and represent an average of the viscosity of the crust in vertical direction. Erosion is not considered so that the calculated crustal thickness represents maximum values and interpretations of the model results in terms of uplift are limited.

[20] It also should be said that the nondimensional model values are here scaled using a nominal length scale of $D =$ 5000 and $U_0 = 5$ cm per year to facilitate the direct comparison with *Houseman and England* [1993]. Velocities and areas shown in Figures 7, 8, 9, and 10 are calculated for these values. However, the model results can be scaled to any other values for D or U_0. Areas increase quadratically with increasing nominal values for D. Viscosities can be directly calculated from equation (4). For the nominal values used here, an Argand number of $Ar = 1$ and a power law exponent of $n = 1$ imply a scaled viscosity of 1.1×10^{22} Pa s. Thus a viscosity contrast of $\eta = 100$ implies that the indenter has a viscosity of 1.1×10^{24} Pa s opposing a foreland with a viscosity of 1.1×10^{22} Pa s. As seen in equation (4), scaled viscosities decrease linearly with increasing Ar and with decreasing nominal values for convergence velocity U_0.

4.1. Tectonic Escape Versus Gravitational Collapse

[21] One of the most exiting aspects of the model presented in the last sections is that it allows to discriminate between the different processes contributing to the process of lateral extrusion. Lateral extrusion is a loosely used term referring to the displacement of rocks normal to the direction of shortening during continental convergence as caused by the combination of tectonic escape and gravitational extensional collapse. Tectonic escape is the forced lateral motion of crustal blocks away from a zone of plate convergence under a regime of overall compression [*Tapponnier et al.*, 1982], while gravitational extensional collapse describes the process of lateral displacement under deviatoric tension along gradients of potential energy [*Dewey*, 1988]. The velocity of material normal to the direction of indentation (u_x) reflects the sum of these two processes. However, the gravitational extensional collapse component can be extracted by looking at two end-member scenarios for which the horizontal velocity field is exclusively related to the process of tectonic escape: (1) the incremental time step (e.g., Figure 7). In all model runs presented in this paper crustal thickness is initially uniform at time zero. Thus there are no gradients in crustal thickness at time zero and the horizontal velocities are therefore due to tectonic forcing only. (2) Argand number is zero: Models for $Ar = 0$ mean that gravity does not act on the orogen that is built during convergence (see equation (4)). Thus the contribution of gravitational collapse to the horizontal velocity field is zero throughout the indentation process, and u_x can be directly interpreted in terms of tectonic escape (e.g., Figure 8a).

[22] To explore the contribution of gravitational extensional collapse onto the horizontal velocity field we have chosen to track the maximum horizontal velocity $u_x^{\max}$ anywhere in the model region. The location of $u_x^{\max}$ changes with elapsed time and the rheological model, but is always located within the foreland as long as $\eta > 1$. It characterizes the behavior of the velocity field better than the temporal evolution of u_x at any particular point of the model region, as these are subject to dramatic changes through time that are unrelated to the processes discussed here. In fact, the central point of the indenter front, useful to characterize the thickness evolution (Figures 4 and 5), will have a horizontal velocity of zero for $\alpha = 0$ (for symmetry reasons) and does not characterize the distribution of tectonic escape at all.
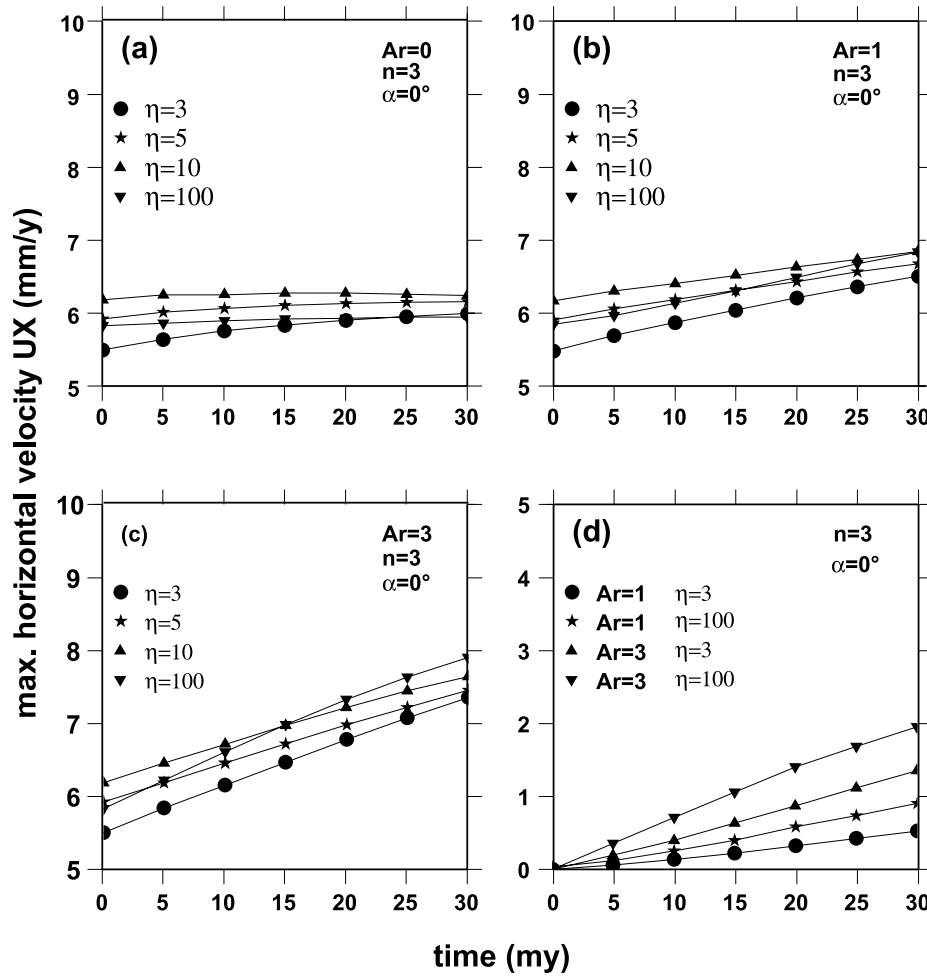
Figure 8. Maximum horizontal velocity u_x^{max} as a function of time during the indentation of rectangular indenter ($\alpha = 0$) with variable viscosity contrast to the foreland as labeled. The power law exponent is $n = 3$ in all figures, and (a) $Ar = 0$, (b) $Ar = 1$, and (c) $Ar = 3$. (d) Effect of the gravitational collapse on u_x^{max} over time calculated by subtracting the values of Figure 8a from the relevant curves in Figures 8b and 8c.

[23] Figure 8 shows the behavior of the horizontal velocity through time for rectangular indenters ($w = D/4$ and $\alpha = 0$). For $Ar = 0$, u_x^{max} remains nearly constant from the onset of the indentation to the final time step at 30 m.y. (Figure 8a). The velocity is controlled by the velocity of indentation. Different viscosity contrasts influence u_x^{max} only to a small extent but softer indenters cause smaller velocities as some of the shortening is compensated by the indenter. Then, the indenter front moves somewhat slower into the foreland. For $Ar = 1$, the effect of the gravitational extensional collapse on the velocity field increases during the indentation process and the overall u_x^{max} increases correspondingly (Figure 8b). This is caused by ongoing crustal thickening and increasingly steeper lateral gradients in the gravitational potential energy field. At $t = 0$, u_x^{max} starts with exactly the same values observed in Figure 8a as there are no gradients in the potential energy field and gravitational collapse is zero. The influence of η remains small (<1 mm y^{-1}). At higher Argand numbers ($Ar = 3$ or greater) the gravitational collapse becomes an important

driving force for horizontal displacement (Figure 8c). A high viscosity contrast ($\eta = 100$) leads to steep gradients in the crustal thickness from the rather undeformed indenter to the highly deformed and thickened foreland and causes therefore highest rates for gravitational extensional collapse. This process is accelerated with elapsed time. For that reason the highest values for u_x^{max} after 30 m.y. of convergence occur in models with great viscosity contrasts.

[24] The component of gravitational collapse to the horizontal velocity can be determined by subtracting the rates of lateral escape (Figure 8a) from the rates shown in Figures 8b and 8c. This is because the rates of tectonic escape remain constant during the whole indentation process and are not influenced by crustal thickening as shown in Figure 8a. This is shown in Figure 8d. As has to be expected, it may be seen that the highest rates for gravitational collapse occur for large Ar and large η. For $Ar = 3$ and $\eta = 100$ the maximum horizontal velocity that is exclusively due to gravitational collapse is about 2 mm y^{-1}. This value is about 4% of the maximum convergence velocity. For low

Argand numbers around $Ar = 1$ and soft indenters with $\eta = 3$, the contribution of gravitational collapse to the lateral extrusion is about 10% of the horizontal displacement rate and 1% of the convergence rate.

[25] The changes of the horizontal velocity field (characterized by u_x^{max}) as a function of indenter angle α are shown
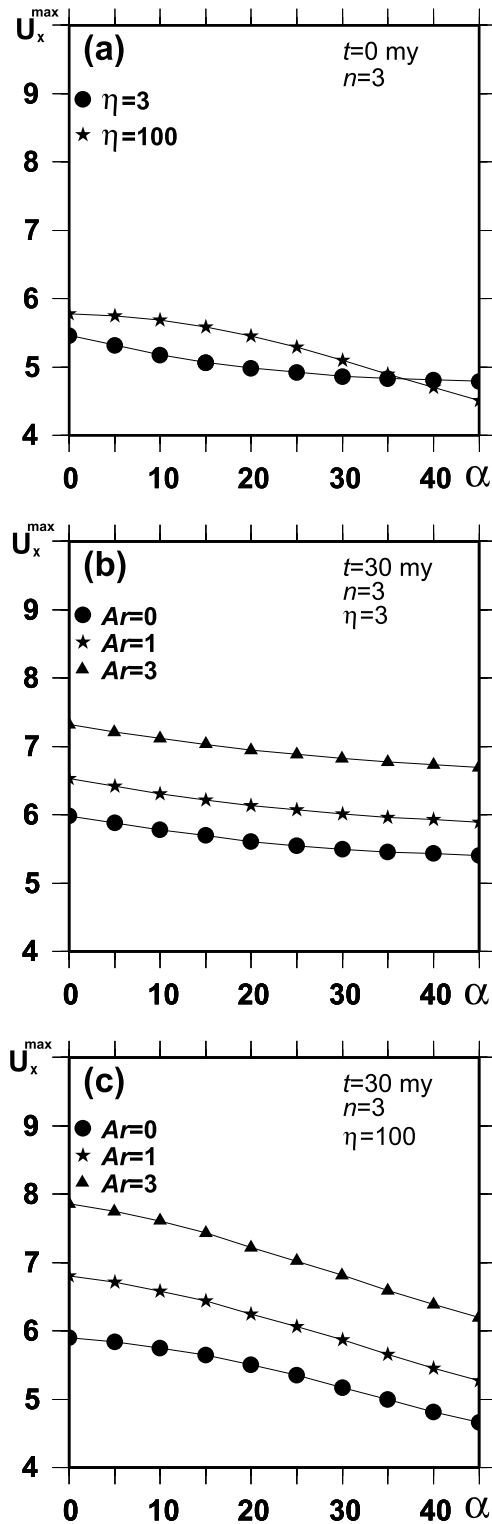
in Figure 9. Several rheology models are explored at $t = 0$ m.y. and $t = 30$ m.y. Interestingly, there is a general decrease of u_x^{max} with increasing α from 0° to 45°. This is because of a corner effect. Indenters with small α have sharp corners causing a rapid eastward motion just near the indenter corner. In contrast, indenters with large α cause a more diffuse eastward displacement. This observation is independent from η. For the incremental time step (Figure 9a), values of u_x^{max} are larger for $\eta = 100$ from $\alpha = 0°$ to $\alpha = 35°$, but larger for $\eta = 3$ from $\alpha = 35°$ to $\alpha = 45°$. The reason for that is that the velocity field becomes highly asymmetric with increasing α for $\eta = 100$. This is not the case for lower viscosity contrasts as shown in Figure 7d. As u_x caused by lateral escape is roughly constant over time, the curves for u_x^{max} do not change shape. They are only shifted by an almost constant value because gravitational extensional collapse is independent of α (Figures 9b and 9c). Thus the difference between the velocities in Figures 9b and 9c to that of Figure 9a can be related exclusively to the process of gravitational extensional collapse and increase in Ar.

4.2. Size of Lateral Extrusion Corridors

[26] In many orogens the extent of the laterally extruding areas is much better known than the absolute velocities. Thus and in view of the somewhat nonintuitive parameter of the maximum horizontal velocity in the x direction, we illustrate here how size of a lateral extrusion corridor develops as a function of indenter angle and time. We focus on the eastward extending corridor and discuss the size of this corridor evolves as a function of time. Figure 10 shows the angle of indentation α plotted against progressive time and contoured for the size of the eastward moving corridor. Scaled to the parameter values used throughout the paper the numbers are in 10^7 km^2. As a measure for "size" we have arbitrarily chosen that area within which the eastward velocity exceeds 1 mm per year. Note that areas increase with the square of length scale. Thus doubling the nominal values for D will result in a four fold increase in the values for the areas discussed here. It may be seen that the size of this area increases with indenter angle, which is to be expected as high angles effectively push the foreland toward the east. This may also be seen by comparing Figures 7a and 7b. The size of the corridor also increases with time, which is due to the successively increasing contribution of gravitational collapse to the lateral displacement field during progressive deformation. The area of the lateral extrusion corridor is less dependent on indenter angle for soft

Figure 9. Relation between the maximum horizontal velocity u_x^{max} in mm per year and the convergence angle α for two different viscosity contrasts and three different rheology models. (a) Plot of α versus u_x^{max} for $\eta = 3$ (dots) and for $\eta = 100$ (stars). Ar does not influence u_x^{max} at $t = 0$ m.y., and no contours for different Ar are therefore drawn. (b) Plot of α versus u_x^{max} for $\eta = 3$ at $t = 30$ m.y. Curves show the influence of $Ar = 0$ (dots), $Ar = 1$ (stars), and $Ar = 3$ (triangles). (c) Plot of α versus u_x^{max} for $\eta = 100$ at $t = 30$ m.y. Curves show the influence of $Ar = 0$ (dots), $Ar = 1$ (stars), and $Ar = 3$ (triangles).
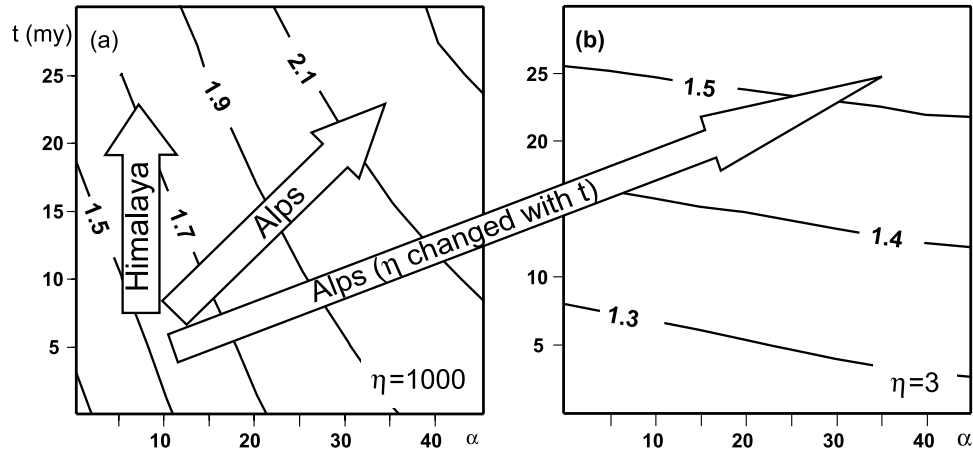
Figure 10. Indentation angle α plotted against time and contoured for the area of an eastward displacing corridor contoured in 10^7 km^2 as appropriate for the nominal parameter values used throughout the paper. Both diagrams are for $Ar = 1$, $n = 3$. The areas are those in which the horizontal velocity u_x exceeds 1 mm per year: (a) viscosity contrast of $\eta = 1000$ and (b) viscosity contrast of $\eta = 3$. The three arrows show schematic paths for the Himalaya and the Alps discussed in the text. Note that the values of the area contours may need scaling for the correct nominal parameter values of any real application.

indenters for reasons discussed above. In fact, the progressive deformation of soft indenters at finite times is reflected in a decreasing dependence of area on angle with time (Figure 10b).

[27] Figure 10 can be used to interpret the size of lateral extrusion corridors through time in orogens. For example, if the indenter has remained normal to the direction of indentation during the entire collision process, then the eastward displacing region increases in size by 20% over time (from 1.5 to 1.7 × 10^7 km^2 for the nominal values for length and timescale used here). Such an area increase may be appropriate to the Himalayas, although the absolute area numbers will need rescaling for the Himalaya. In contrast, in orogens like the eastern European Alps, *Frisch et al.* [1998] suggested that the Adriatic indenter commenced as a square front in the Oligocene and developed its present oblique geometry during progressive rotation over the last 30 m.y. Figure 10a shows that this implies a much larger increase of the eastward displacing corridor during this evolution of around 50%. On the other hand, if the indenter softened (relative to the foreland) during its indentation history (and there is strong evidence for a reduction of the rheology contrast [*Robl and Stüwe*, 2005] then the area of the corridor may have stayed roughly constant (compare top right corner of Figure 10a with Figure 10b). While such speculations could be used to provide very exciting constraints on the changes in rheology of the Adriatic indenter through time, they may not be justified in the light of the ill-constrained nature of the processes involved. These processes are discussed in a more refined model in the companion paper [*Robl and Stüwe*, 2005].

4.3. Interpreting Thickening Rates

[28] In principle, Figures 4 and 5 can be used to estimate aspect ratio and rheology of an indenter during

continental collision. Figure 5 shows only the contour for an even distribution of crustal thickness between indenter and foreland, but contours for other thickness ratios can be drawn on this diagram. Present day crustal thicknesses are the product of a complicated evolution of thickness through time and are difficult to interpret on this diagram. However, in isostatic equilibrium, the changes of crustal thickness are reflected in surface uplift rate, a parameter that may and is being measured. Rates of surface uplift relate to rates of crustal thickening by the density contrast between crust and mantle. On the most simple level it may be interpreted to relate by $\delta H/\delta t = \delta S/\delta t \, (1 - \rho_c/\rho_m)$ where H is surface elevation and the other parameters are as described above. For example, using the nominal values of Figure 4a it may be seen that the thickening rate is about 30 km in 50 m.y. With the values for densities used above, this predicts an uplift rate of about 0.077 mm y^{-1}. While these absolute numbers not only change with the nominal scaling values, but also are subject to large errors, the ratio of uplift rate between indenter and foreland are identical to those of crustal thickness. Thus ratios of uplift rates may be a useful parameter to infer aspects of the size and rheology of indenters. On the other hand, it must be said that uplift rates in orogens are unlikely to be governed by isostatically compensated processes. A variety of studies has shown that the surface uplift rates in collision zones are largely proportional to erosion rates, while the influence of isostatic compensation is small [*Lave and Avouac*, 2001].

5. Conclusion

[29] The rheology of a continental indenter is crucial to the development of an orogen because it determines the partitioning of deformation between the indenter and its

foreland. The partitioning is strongly dependent on the viscosity contrast between indenter and foreland, the aspect ratio of the indenter and the angle of indentation.

[30] The majority of deformation occurs within the indenter, if viscosity of the indenter is small and the aspect ratio of this low-viscosity region is large. In contrast, stresses are transmitted into the foreland if the viscosity contrast is large and the indenter narrow. For indenters that are twice as viscous as their foreland, an aspect ratio of 2:1 will cause roughly equal partitioning of crustal thickening between indenter and foreland for a range of Argand numbers and power law exponents. For indenters that are ten times as viscous as their foreland, the aspect ratio must be 1 so that crustal thickening is partitioned equally between indenter and foreland (at $n = 3$ and $Ar = 1$). However, for large viscosity contrasts, the partitioning is strongly dependent on power law exponent and Argand number.

[31] The angle of indentation α alters the thickening and velocity pattern in the foreland significantly. During oblique indentation the distribution of crustal thickening remains roughly symmetric about the oblique indenter front. However, the horizontal velocity field in the foreland becomes highly asymmetric. If the indenter is less than 10 times as viscous as the foreland, it becomes rapidly deformed during progressive deformation so that the thickening and horizontal velocity fields approach that of rectangular indenters after time.

[32] The process of lateral extrusion is interpreted by tracking the maximum horizontal velocity $u_x^{\max}$ through time. $u_x^{\max}$ remains roughly constant over time for $Ar = 0$ as lateral escape is not influenced by crustal thickening. $u_x^{\max}$ increases gradually with time for larger Ar as gravitational extensional collapse provides an increasing contribution to the lateral velocity field. After 30 m.y. of convergence the gravitational extensional collapse accounts for about 1/3 of $u_x^{\max}$ at $\eta = 100$ but is less important for smaller η. Areas with significant east directed lateral motion increase with indenter angle, but the lateral gradient of u_x is smooth. In contrast the gradient of u_x is steep west of the indenter and $u_x^{\max}$ in the domains east and west of the indenter are in the same order of magnitude, but show the lowest values for all explored collision geometries.

[33] Rough comparison with the India Asia collision zone predicts that the area of eastward displacement has increased by about 20% since the onset of collision. In contrast, in the European Alps, where the indenter has probably changed its obliquity over the last 30 m.y. [*Frisch et al.*, 1998], the area may have increased by about 50% during this time interval. However, if the indenter softened during indentation, as indicated by the strong current seismicity within the Adriatic plate, then the area increase of the lateral extrusion corridor may not be so dramatic.

References

Babbucci, D., C. Tamburelli, M. Viti, E. Mantovani, D. Albarello, F. D'Onza, N. Cennni, and E. Mugnaioli (2004), Relative motion of the Adriatic with respect to the confining plates: Seismological and geodetic constraints, *Geophys. J. Int.*, *159*, 765–775.

Barr, T. D., and G. A. Houseman (1996), Deformation fields around a fault embedded in a non-linear ductile medium, *Geophys. J. Int.*, *125*, 473–490.

Beaumont, C., S. Ellis, J. Hamilton, and P. Fullsack (1996), Mechanical model for subduction-collision tectonics of Alpine-type compressional orogens, *Geology*, *24*, 675–678.

Bird, P., and K. Piper (1980), Plane-stress finite-element models of tectonic flow in southern California, *Phys. Earth Planet. Inter.*, *21*, 158–175.

Bonini, M., D. Sokoutis, C. J. Talbot, M. Boccaletti, and A. Milnes (1999), Indenter growth in analogue models of Alpine-type deformation, *Tectonics*, *18*, 119–128.

Bressan, G., A. Snidarcig, and C. Venturini (1998), Present state of tectonic stress of the Friuli area, *Tectonophysics*, *292*, 211–227.

Dewey, J. F. (1988), Extensional collapse of orogens, *Tectonics*, *7*, 1123–1139.

England, P. C., and G. A. Houseman (1986), Finite strain calculations of the continental deformation: 2. Comparison with the India-Asia collision zone, *J. Geophys. Res.*, *91*, 3664–3676.

England, P. C., and D. McKenzie (1982), A thin viscous sheet model for continental deformation, *Geophys. J. R. Astron. Soc.*, *70*, 295–321. (Correction, *Geophys. J. R. Astron. Soc.*, *73*, 523–532, 1983.)

Frisch, W., J. Kuhlemann, I. Dunkl, and A. Brügel (1998), Palinspastic reconstruction and topographic evolution of the Eastern Alps during late Tertiary tectonic extrusion, *Tectonophysics*, *297*, 1–15.

Frisch, W., I. Dunkl, and J. Kuhlemann (2000), Post-collisional large-scale extension in the Eastern Alps, *Tectonophysics*, *327*, 239–265.

Gerbault, M., and E. Willingshofer (2004), Lower crust indentation or horizontal ductile flow during continental collision?, *Tectonophysics*, *387*, 169–187.

Harrison, T. M., P. Copeland, W.S.F. Kidd, and A. Yin (1992), Raising Tibet, *Science*, *255*, 1663–1670.

Houseman, G. A., and P. C. England (1986), Finite strain calculations of continental deformation: 1. Method and general results for convergent zones, *J. Geophys. Res.*, *91*, 3651–3663.

Houseman, G. A., and P. C. England (1993), Crustal thickening versus lateral expulsion in the India-Asian continental collision, *J. Geophys. Res.*, *98*, 12,233–12,249.

Keep, M. (2000), Models of lithospheric-scale deformation during plate collision: Effects of indentor shape and lithospheric thickness, *Tectonophysics*, *326*, 203–216.

Lave, J., and J. P. Avouac (2001), Fluvial incision and tectonic uplift across the Himalayas of central Nepal, *J. Geophys. Res.*, *106*, 26,561–26,591.

Marotta, A. M., U. Bayer, H. Thybo, and M. Scheck (2002), Origin of the regional stress in the north German basin: Results from numerical modelling, *Tectonophysics*, *360*, 245–264.

Medvedev, S., and Y. Y. Podladchikov (1999), New extended thin-sheet approximation for geodynamic applications: I. Model formulation, *Geophys. J. Int.*, *136*, 567–585.

Molnar, P., and P. Tapponnier (1975), Cenozoic tectonics of Asia: Effects of a continental collision, *Science*, *189*, 419–426.

Neil, A. E., and G. A. Houseman (1997), Geodynamics of the Tarim basin and the Tien Shan in central Asia, *Tectonics*, *16*, 571–584.

Pfiffner, O. A., S. Ellis, and C. Beaumont (2000), Collision tectonics in the Swiss Alps: Insight from geodynamic modeling, *Tectonics*, *19*, 1065–1094.

Platt, J. P. (1993), Mechanics of oblique convergence, *J. Geophys. Res.*, *98*, 16,239–16,256.

Ratschbacher, L., W. Frisch, F. Neubauer, S. M. Schmid, and J. Neugebauer (1989), Extension in compressional orogenic belts: The Eastern Alps, *Geology*, *17*, 404–407.

Ratschbacher, L., O. Merle, P. Davy, and P. Cobbold (1991), Lateral extrusion in the Eastern Alps: 1. Boundary conditions and experiments scaled for gravity, *Tectonics*, *10*, 245–256.

Robl, J. and K. Stüwe (2005), Continental collision with finite indenter strength: 2. European Eastern Alps, *Tectonics*, doi:10.1029/2004TC001741, in press.

Royden, L. (1996), Coupling and decoupling of crust and mantle in convergent orogens: Implications for strain partitioning in the crust, *J. Geophys. Res.*, *101*, 17,679–17,705.

Shen, F., L. H. Royden, and B. C. Burchfiel (2001), Large-scale crustal deformation of the Tibetan Plateau, *J. Geophys. Res.*, *106*, 6793–6816.

Shewchuck, J. R. (2002), Delaunay refinement algorithms for triangular mesh generation, *Comput. Geometry Theory Appl.*, *22*, 21–74.

Sobouti, F., and J. Arkani-Hamed (1996), Numerical modelling of the deformation of the Iranian Plateau, *Geophys. J. Int.*, *126*, 805–818.

Soofi, M. A., and S. D. King (2002), Post-rift deformation of the Midcontinent rift under Grenville tectonism, *Tectonophysics*, *359*, 209–223.

Tapponnier, P., G. Peltzer, A. Y. Le Dain, R. Armijo, and P. Cobbold (1982), Propagating extrusion tectonics in Asia: New insights from simple experiments with plasticine, *Geology*, *10*, 611–616.

Tenczer, V., K. Stüwe, and T. D. Barr (2001), Pressure anomalies around cylindrical objects in simple shear, *J. Struct. Geol.*, *23*, 777–788.

Viola, G., N. S. Mancktelow, and D. Seward (2001), Late Oligocene-Neogen evolution of Europe-Adria collision: New structural and geochronological evidence from the Guidicarie fault system (Italian Eastern Alps), *Tectonics*, *20*, 999–1020.

Willingshofer, E., D. Sokoutis, and J.-P. Burg (2004), Influence of the initial geometry of lateral strength variations during continental convergence: An analogue modelling study, *Boll. Geofis.*, *45*, 164–168.

J. Robl and K. Stüwe, Institut für Erdwissenschaften, Universität Graz, Heinrichstr. 26, A-8010 Graz, Austria. (joerg.robl@uni-graz.at)